In situ radiographic and ex situ tomographic investigation of pore collapse in laser shock-loaded polyurethane foam

P. Pradel, T. de Rességuier, F. Malaise, M P Olbinado, A. Rack, J. Grenzer, D. Loison, L. Berthe

Journal of Applied Physics

RESEARCH ARTICLE | FEBRUARY 02 2022

In situ radiographic and *ex situ* tomographic investigation of pore collapse in laser shock-loaded polyurethane foam

P. Pradel ✉; T. de Rességuier; F. Malaise; ... et. al

Journal of Applied Physics 131, 055106 (2022)
https://doi.org/10.1063/5.0077613

Journal of Applied Physics ARTICLE scitation.org/journal/jap

In situ radiographic and *ex situ* tomographic investigation of pore collapse in laser shock-loaded polyurethane foam

Cite as: J. Appl. Phys. **131**, 055106 (2022); doi: 10.1063/5.0077613
Submitted: 4 November 2021 · Accepted: 15 January 2022 ·
Published Online: 2 February 2022

P. Pradel,[1,a] T. de Rességuier,[2] F. Malaise,[1] M. P. Olbinado,[3] A. Rack,[3] J. Grenzer,[4] D. Loison,[5] and L. Berthe[6]

AFFILIATIONS

[1]CEA CESTA, 15 avenue des Sablières CS60001, 33116 Le Barp Cedex, France
[2]Institut Pprime UPR3346 CNRS-Université de Poitiers-ENSMA, 11 boulevard Marie et Pierre Curie, 86962 Futuroscope Chasseneuil Cedex, France
[3]ESRF—The European Synchrotron, CS40220, 38043 Grenoble Cedex 9, France
[4]Helmholtz-Zentrum Dresden-Rossendorf, Bautzner Landstrasse 400, D-01328 Dresden, Germany
[5]Univ Rennes, CNRS, IPR (Institut de Physique de Rennes)—UMR 6251, F-35000 Rennes, France
[6]PIMM, UMR8006 ENSAM, CNRS, CNAM, 151 bd de l'Hôpital, 75013 Paris, France

Note: This paper is part of the Special Topic on Shock Behavior of Materials.
[a]**Author to whom correspondence should be addressed:** pierre.pradel@cea.fr

ABSTRACT

Laser-driven shock experiments were conducted at a synchrotron facility to investigate the dynamic response of polyurethane foam. These experiments were coupled to *in situ* x-ray imaging to radiograph foam deformations and to determine the propagation velocity of stress waves. To increase the amplitude and the duration of the pressure load generated by the laser–matter interaction, the front surface of the target was covered with a confining layer (water and BK7 glass). Preliminary calibration tests involving time-resolved velocity measurements were performed to calculate the ablation pressure on the front surface of foam samples. The calculated pressure loads were used as input data for hydrodynamic simulations, in which the foam is modeled using a homogeneous porous macroscopic model, and model predictions were compared with experimental results. A fair consistency was found for most experiments, while for the others, an overestimation of the applied pressure is suspected, likely due to a laser breakdown within the confining medium. Finally, post-shot x-ray tomography of the recovered samples showed permanent deformation of the foam, unlike what was observed under quasi-static compression, and revealed heavy damage in the vicinity of the loaded zone.

I. INTRODUCTION

Cellular materials, such as polymeric foams, are widely used for their energy absorption abilities for cushioning applications in various industrial contexts, such as automotive, aerospace, and defense fields.[1] An application of particular interest is the protection of diagnostics (velocity, temperature measurements, etc.) and optics (mirrors, lenses, etc.) against dynamic loadings inside the vacuum chamber in large scale laser facilities such as the Laser MégaJoule (LMJ) or the National Ignition Facility (NIF). These devices may indeed be subjected to laser irradiation and/or impact of small debris that can generate intense (several gigapascals) and brief (a few nanoseconds) stress waves. One solution to mitigate the effects of this type of solicitation is to insert an absorbing material between a screen whose role is to stop the laser beam or debris and the component to be protected. In this context, understanding deformation mechanisms during the propagation of intense stress waves in a porous material is of great importance for analyzing its mitigation ability.

In this study, we focus on the dynamic behavior of a rigid closed-cell polyurethane foam subjected to laser-driven shock loading. The mechanical behavior of polyurethane foams has already been studied for different strain rates. This characterization includes drop weight tower experiments,[2–5] Split Hopkinson Pressure Bar (SHPB) tests,[6–11] gas gun experiments,[12–17] and electron beam tests.[17,18] To complement this exploration and extend it to higher strain rates relevant to the aforementioned context, we used laser-driven shocks to generate stress pulses of duration lower than 100 ns. The experiments were performed at the European Synchrotron Radiation Facility (ESRF), using the bright x-ray source for *in situ* radiography of the foam deformations during the propagation of the stress waves. The analysis of x-ray radiographs allows us to calculate the propagation velocity of these waves; then, post-recovery characterization using both microscopy and x-ray tomography provides the state of the foam after shock propagation. A macroscopic compaction model is used to simulate the foam behavior under dynamic loading,[16–18] and simulations are compared with experimental results.

II. MATERIAL

The polyurethane foam was obtained by blending a diisocyanate—methylene diphenyl diisocyanate (MDI)—with a diol. The addition of water during the polymerization reaction produces carbon dioxide creating spherical porosities of diameter between a few tens and a few hundreds μm. A tomographic analysis of the structure of the foam shows the presence of small holes interconnecting pores to each other (Fig. 1). Nevertheless, these holes are small enough to consider that the foam is essentially closed-cell. The polyurethane foam has a density ρ_0 of 320 ± 20 kg/m^3. The porosity deduced from the tomographic analysis is 66%. According to literature data,[1,19] the density ρ_{0s} of dense polyurethane is 1240 ± 40 kg/m^3. The definition of porosity ($\phi_0 = 1 - \rho_0/\rho_{0s}$) gives an initial porosity of about 75%, different from the one obtained by tomographic analysis. One possible explanation is that the actual matrix density is not 1264 kg/m^3, because the polyurethane was not obtained under the same conditions. As an indication, to obtain a porosity of 66%, the matrix should have a density of around 1000 kg/m^3.

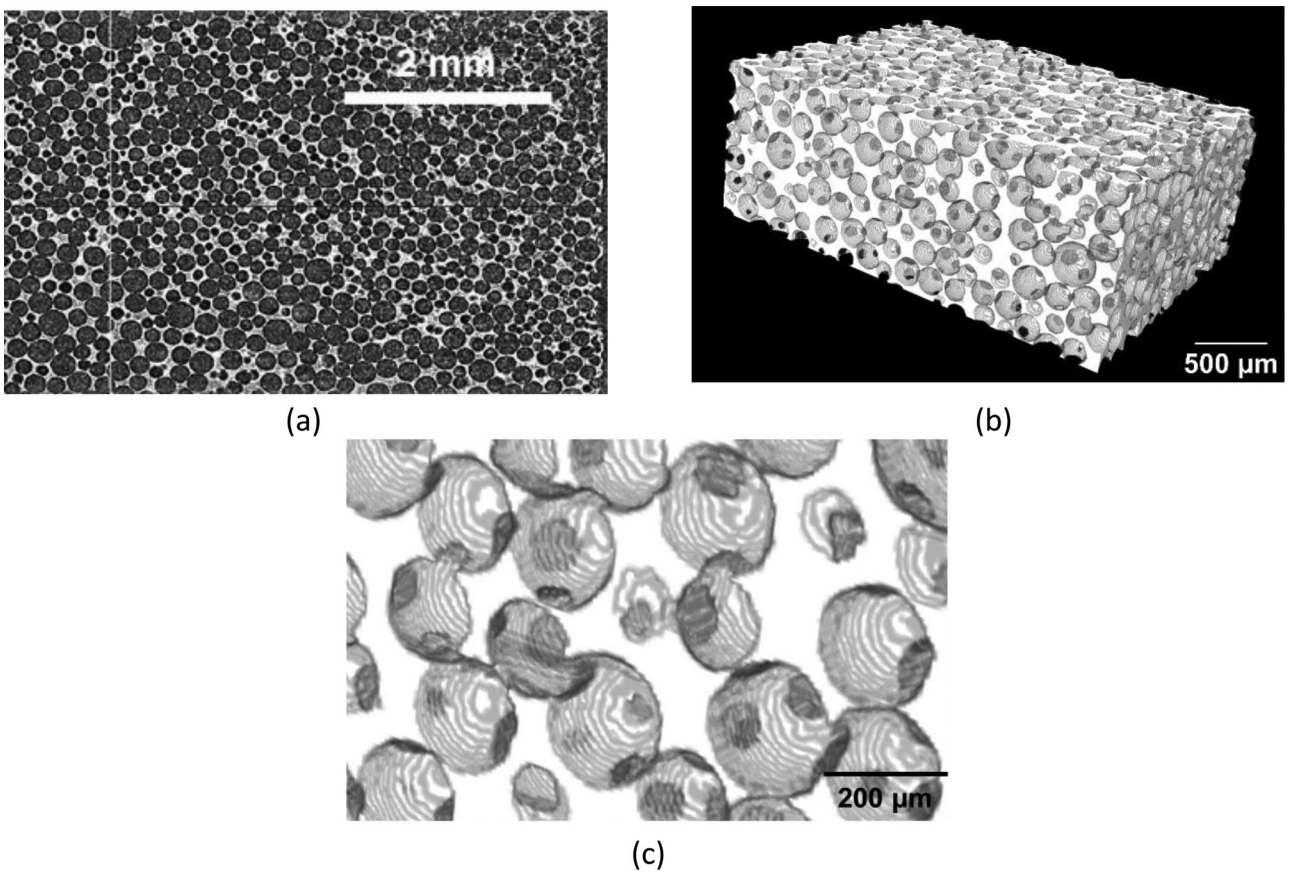

FIG. 1. Initial mesostructure of the polyurethane foam: 2D section extracted from x-ray tomography (a), 3D x-ray tomography (b), and closer view (c) showing the presence of small holes interconnecting pores to each other.

III. EXPERIMENTAL SETUP

The European Synchrotron Radiation Facility (ESRF) in Grenoble (France) is a synchrotron of the third generation type. Electrons are accelerated at the speed of light in the synchrotron then deflected to create x rays. Experiments were performed at the microtomography beamline ID19 of the ESRF. A schematic overview of the experimental setup is shown in Fig. 2. More details on this setup can be found in Refs. 20 and 21. In our experiments, x-ray phase-contrast imaging (XPCI) is used. Compared to x-ray radiography based on attenuation-contrast, this technique permits to enhance the visibility of discontinuities, such as density variations due to the propagation of a shock wave.[22] The 16-bunch filling mode of the storage ring is used. Each x-ray pulse has a duration of about 100 ps full width at half maximum (FWHM); the time between x-ray flashes is 176 ns. The average x-ray energy is about 30 keV, with a maximum flux of 20×10^6 photons/mm^2/pulse. After passing through the foam sample, x-ray pulses are detected using a fast-decay scintillator [250 μm-thick Ce-doped $(Lu_{(2-x)}Y_x)SiO_5$ (LYSO:Ce), Hilger Crystals, UK], lens-coupled to an ultra-high-speed visible light camera (Hyper Vision HPV-X2, Shimadzu Corp., Japan). 128 images are stored in one recording sequence with an effective pixel size of 8 μm. In order to avoid empty frames and achieve full exploitation of the 128 images, an inter-frame of 530 ns is used in experiments, which means that one in three x-ray pulses is detected. The field of view is 3.2×2 mm^2.

The synchronization between the laser pulse, x-ray pulses, and the imaging detector is essential for monitoring the propagation of waves into the material. To this end, the ESRF radio frequency (RF) system was first used as a master clock signal. A Quad 4-input logic unit was used to synchronize the laser and x-ray pulses. Delay generators (DGs) were used to calibrate delays of the trigger signals to the laser flashlamp, the laser Q-switch, and the ultra-high-speed camera. The delay value for the camera trigger was chosen so that the laser/x-ray coincidence corresponds to the third image (Fig. 3).[20]

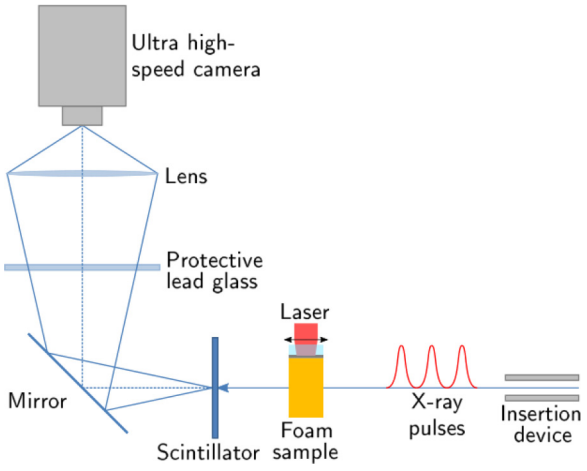

FIG. 2. Experimental setup for laser-driven shock experiments performed at the ESRF. After crossing the foam sample, x-ray pulses are detected using a LYSO:Ce scintillator and a HPV-X2 Shimadzu ultra-high-speed camera.

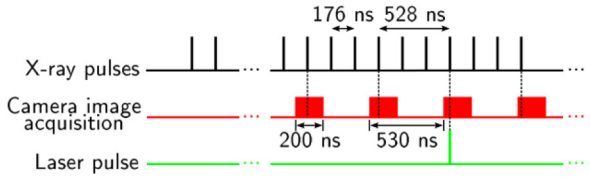

FIG. 3. Timing scheme. The ESRF RF system served as a master clock. The synchronization between the laser and x-ray pulses was realized using an input logic unit. Time delays of the trigger signals to the laser flashlamp, the laser Q-switch, and the ultra-high-speed camera were tuned using DGs.

The target consists of a 4×4 mm^2 square section foam sample of thickness between 2 and 5 mm, coated with a 12 μm-thick aluminum foil on its top surface. A laser pulse is focused on a 2–3 mm diameter spot in this aluminum foil. The thin absorbing layer (a few μm-deep) of aluminum is transformed into a plasma cloud, whose expansion generates, by reaction, a shock wave, which is transmitted into the foam. Assuming a spatially uniform energy distribution in the laser beam and disregarding the foam heterogeneity, conditions of uniaxial strain, i.e., 1D propagation of planar wave fronts, can be expected in the central region, before the arrival of lateral release waves coming from the periphery of the loaded spot. The aluminum foil is covered with a dielectric transparent to laser irradiation (water or BK7 glass). This confinement limits the expansion of the plasma (Fig. 4) and increases the amplitude and the duration of the pressure load.[23] However, the presence of this confinement bounds the laser intensity below a so-called breakdown threshold. Indeed, above this threshold intensity, the confining medium (air, water, glass) between the source and the target is ionized and absorbs the laser energy, which is no longer deposited into the target.

The pressure load applied on the top face of aluminum is of compression-release type with a FWHM of about twice the laser pulse duration, due to the confinement. Calibration shots were dedicated to the determination of this pressure load (Sec. IV A).

The GAIA-I laser (GAIA-I, flash lamp-pumped Nd:YAG, Thales LAS, France) was used in single pulse mode. The maximum energy E of this laser is about 5 J, the wavelength λ is 532 nm, and the pulse duration τ is around 10–12 ns.

The main experimental parameters are listed in Table I. For each shot, the laser energy E is determined from a mirror leak, using a calorimeter, and the spot diameter D is inferred from low energy shots on a thermosensitive paper. $I_0 = 4E/\tau\pi D^2$ corresponds to the shot intensity.

IV. EXPERIMENTAL RESULTS AND DISCUSSION

A. Determination of the pressure loads

To quantitatively interpret the dynamic behavior of the foam, the pressure load must be evaluated. This requires either an analytical description of laser–matter interaction in confined geometry or time-resolved measurements in addition to *in situ* radiography (which does not give direct access to the pressure). As no such measurements could be achieved in the experiments performed at

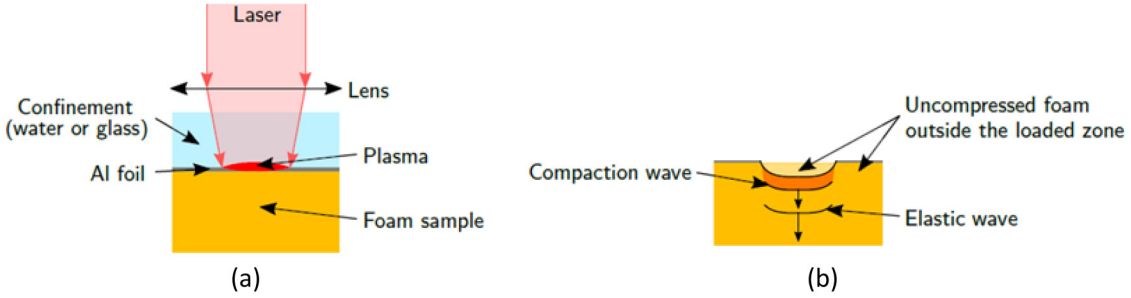

FIG. 4 Schematic description of laser shock loading of the multi-layered target (a) and wave propagation in the foam sample probed by x rays (b).

the ESRF, due to logistic issues and equipment availability, preliminary shots dedicated to load calibration were performed under similar laser irradiation conditions at the Institut Pprime.

The corresponding laser can deliver pulses of maximum energy up to 20 J at 1.053 μm-wavelength, with a pulse duration of 25 ns FWHM. The laser spot diameter was about 6 mm. Laser shots were performed on 250 μm-thick aluminum samples with water confinement, using a Velocity Interferometer System for Any Reflector (VISAR) to measure free surface velocity profiles at the rear surface of aluminum (Fig. 5). Shot parameters are given in Table II.

Typical velocity records are plotted as solid black lines in Figs. 6(b)–6(d). They start with a steep acceleration upon shock breakout (at about 70 ns), followed by oscillations due to the reverberation of waves between the front surface and the rear surface of the sample. The ablation pressure profiles are determined by a reverse approach. The maximum pressure, the pulse duration, and the shape of the release are fitted to reproduce, by 1D numerical simulations, the velocity records. Thus, the pressure profiles shown in Fig. 6(a) give the velocity profiles plotted in red dashed lines in Figs. 6(b)–6(d). Their good match with the records validates the ablation pressure profiles for laser energies between 9 and 17 J.

TABLE I. List of the experiments performed at the eSRF. e is the foam thickness, e is the laser energy, d is the diameter of the irradiated spot and i_0 is the laser intensity.

Shot	Thickness e (mm)	Confinement	Energy E (J)	Spot diameter D (mm)	Intensity I_0 (GW/cm^2)
#1	5.00	Water	3.50	3.00	4.95 ± 0.18
#2	5.00	Water	3.80	3.00	5.38 ± 0.19
#3	5.00	Water	3.80	3.00	5.38 ± 0.19
#4	5.00	Water	1.90	3.00	2.69 ± 0.10
#6	2.38	Water	1.83	1.70	8.06 ± 0.52
#7	5.00	Glass	1.95	1.70	8.59 ± 0.55
#9	1.88	Glass	1.87	2.05	5.67 ± 0.31
#10	5.00	Glass	0.70	2.60	1.32 ± 0.07

An analytical model was developed by Fabbro *et al.*[24] to predict laser-driven shock pressures in the confined regime. It describes the three different phases occurring for confined plasma—laser heating, adiabatic cooling, and final expansion—and permits to estimate the pressure inside the confined plasma. The peak pressure generated by the laser plasma is given by the following formula:

$$P\ (\mathrm{GPa}) = 0.01\sqrt{\frac{\alpha}{2\alpha+3}}\sqrt{Z\ (\mathrm{g/cm^2\ s})}\sqrt{I_0\ (\mathrm{GW/cm^2})}, \quad (1)$$

where α is the fraction of the internal energy devoted to the thermal energy (typically between 0.1 and 0.3), and Z is the reduced shock impedance between the target and the confinement defined by the formula

$$\frac{2}{Z} = \frac{1}{Z_{confinement}} + \frac{1}{Z_{target}}, \quad (2)$$

where $Z_{confinement}$ and Z_{target} are the shock impedances (i.e., product of density and bulk sound velocity), respectively, of the confinement (water, $Z_{water} = 1.65 \times 10^5$ g/cm^2 s, and glass, $Z_{glass} = 1.3 \times 10^6$ g/cm^2 s) and of the target. For calibration tests, the target is aluminum ($Z_{aluminum} = 1.5 \times 10^6$ g/cm^2 s). For ESRF experiments, the aluminum foil is partially ablated and its

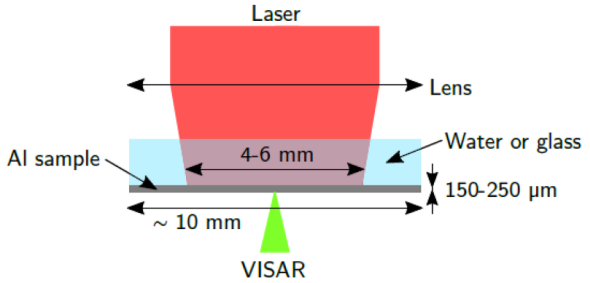

FIG. 5. Laser-driven shock tests performed at the Institut Pprime on aluminum. The free surface velocity was monitored with a VISAR represented by the green beam.

TABLE II. List of the calibration tests performed at the Institut Pprime.

Shot	Thickness e (μm)	Confinement	Energy E (J)	Pulse duration τ (ns)	Spot diameter D (mm)	Intensity I_0 (GW/cm^2)
Al#1w	250	Water	16.92	25.0	6.0	2.39 ± 0.17
Al#2w	250	Water	12.50	30.0	4.0	3.32 ± 0.35
Al#3w	250	Water	12.97	25.0	6.0	1.83 ± 0.13
Al#4w	250	Water	9.40	25.0	6.0	1.33 ± 0.10
Al#5w	250	Water	12.40	30.0	4.0	3.29 ± 0.34
Al#6w	150	Water	20.10	33.4	4.0	4.79 ± 0.50
Al#7w	250	Water	16.70	34.0	5.0	2.50 ± 0.21
Al#1g	250	Glass	8.60	34.5	4.0	1.98 ± 0.21
Al#2g	250	Glass	8.80	40.4	4.0	1.73 ± 0.18

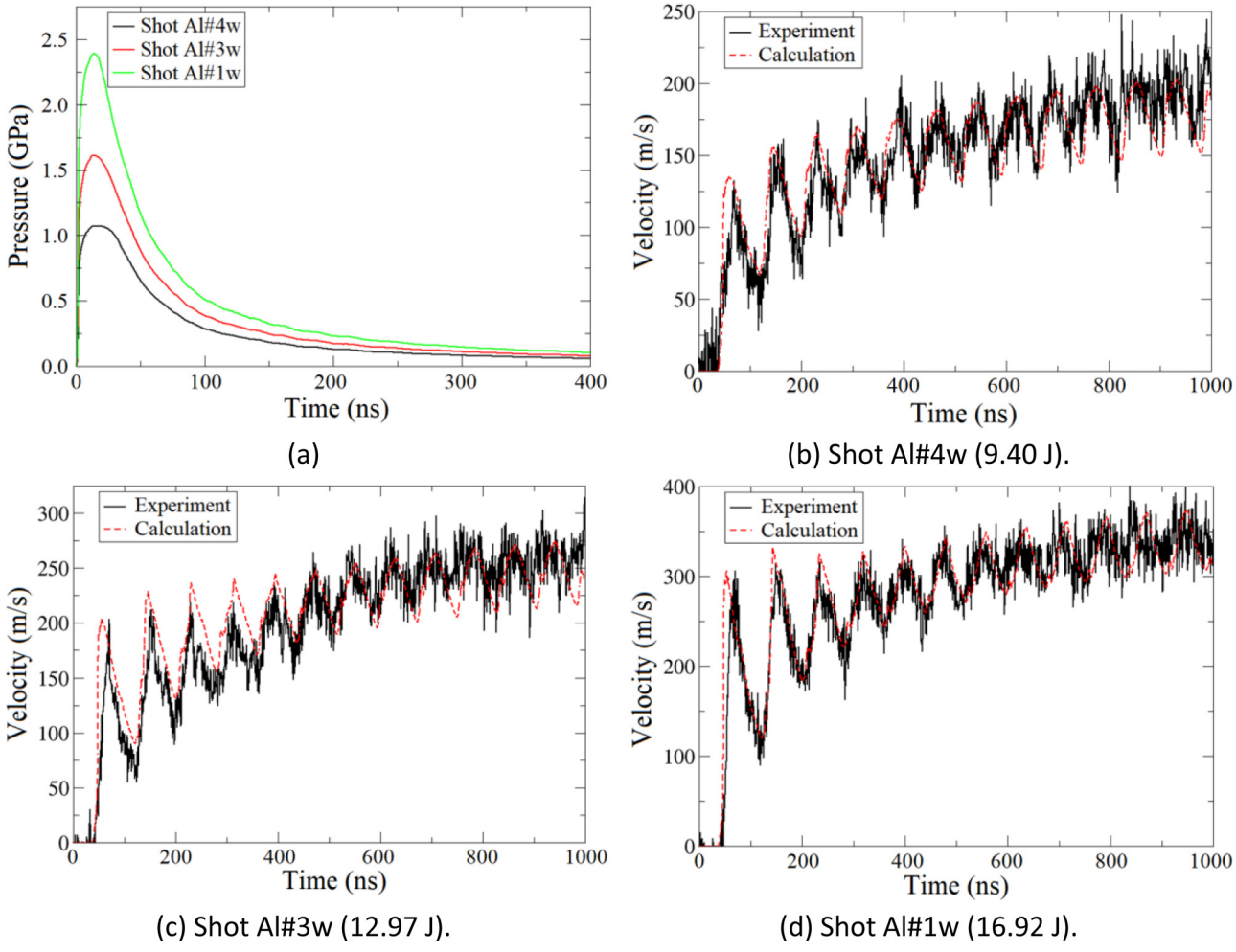

FIG. 6. Loading pressure profiles for three typical laser shots (a) obtained from comparisons between calculated and measured velocity profiles at the free surface of aluminum samples (b)–(d).

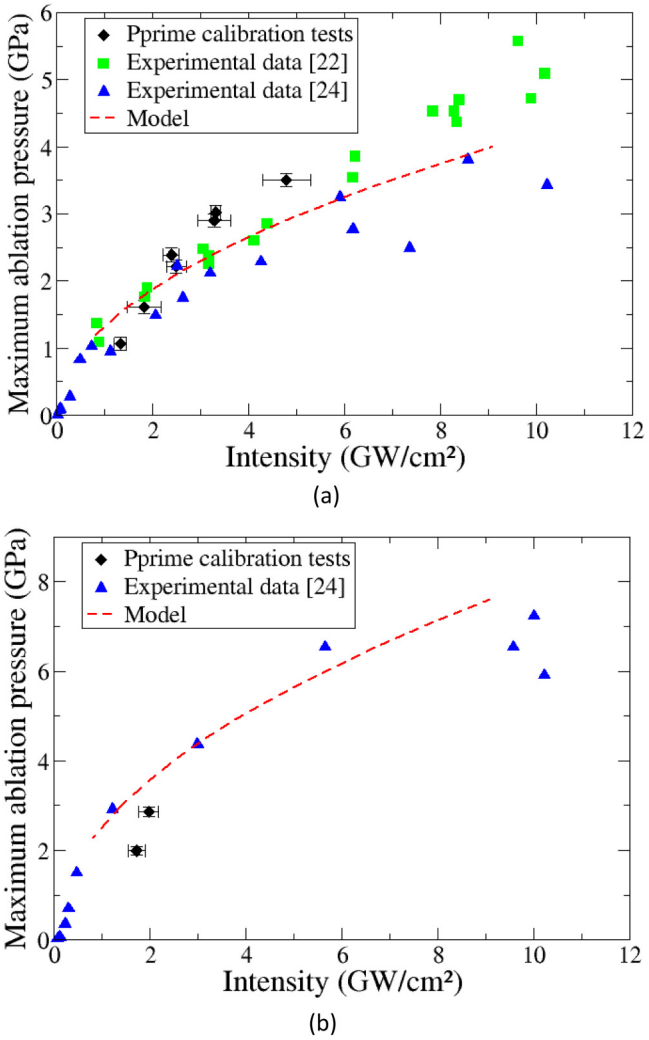

FIG. 7. Maximum ablation pressure measurements as a function of intensity for water confinement and comparison with the analytical model (with $\alpha = 0.2$) (a); for glass confinement and comparison with the analytical model (with $\alpha = 0.15$) (b).

remaining thickness is small enough to be neglected. In this case, the target is the foam ($Z_{foam} = \rho_0 \times C_0 = 4.0 \times 10^4$ g/cm^2 s, with $\rho_0 = 320$ kg/m^3 and $C_0 = 1250$ m/s; cf. Sec. V A). In both cases, the material ablated into plasma is aluminum, so the α coefficient describing the thermomechanical efficiency of the laser–matter interaction in Eq. (1) is expected to be the same.

In Fig. 7, peak pressure values obtained from Eq. (1) (with $\alpha = 0.2$ for water confinement and $\alpha = 0.15$ for glass confinement)[25] are compared with loading pressures inferred from the calibration tests and with relevant data from the literature under water-confined interaction[23] and glass-confined geometry.[25] A fair overall consistency is found, despite significant scatter.

This correct consistency allows us to estimate the loading pressures in our ESRF experiments using Eq. (1) with the same α values and the laser intensity measured at each shot. These pressures are given in Table III. Using the model described in Sec. V A, calculated strain rates are about 9.5×10^5 s^{-1}, which is quite high compared to SHPB or gas gun experiments but typical of laser-driven shock compression in confined geometry.

According to Berthe *et al.*,[23] the breakdown threshold for laser pulses at 1.06 μm in a water-confined regime is about 10 GW/cm^2 for pulse durations between 25 and 30 ns. Sollier[26] showed that the pulse duration has an influence on the threshold but not between 10 and 25 ns. Furthermore, the threshold diminishes with the laser wavelength:[27] at 532 nm, the pressure saturates at a constant level above an intensity threshold of 6 GW/cm^2.

For BK7 glass, the breakdown threshold is estimated to be 3 GW/cm^2 for a 30 ns pulse, and 8 GW/cm^2 for a 3 ns pulse, at 1.06 μm.[25] Like for water confinement, one can estimate that the threshold for a pulse duration of 10–12 ns is roughly the same as for 30 ns. Smith *et al.*[28] showed that the glass breakdown threshold at 532 nm was slightly different from that at 1064 nm (factor 1.08 between breakdown threshold electric fields at 532 and 1064 nm).

Hence, in the shots of highest intensities (#6 and #7), a breakdown in the dielectric is possible, which has the consequence to saturate the peak pressure, and reduce the pulse duration, as will be discussed next. Shots #1, #4, and #10 are not mentioned further in this paper because the pressure was too low to see a compaction wave propagate. For shot #3, the scintillator broke and no image was recorded. However, the sample was recovered.

B. *In situ* x-ray radiography

Figure 8 shows *in situ* radiography of polyurethane foams subjected to laser shock loading on their top surface [see Fig. 4(b)]. As explained in Sec. III, these radiographs are separated by 530 ns. The interaction between the laser and the aluminum foil generates a shock, which propagates into the foam, from the top to the bottom, splitting into a two-wave structure: first an elastic wave, called elastic precursor, due to the elastic response of the polymeric matrix, and then a compaction wave associated to pore collapse under further compression. The propagation velocity of the elastic precursor is higher than that of the compaction wave, according to both theoretical and model predictions.[29]

Phase-contrast x-ray images of highly porous materials such as the foam samples under study are rendered visible due to the refraction at interfaces of the cell edges. Due to the large amount of pores along the beam path, the fringe patterns of the different lamellae overlap, forming a speckle-like pattern on the detector. When elastic and compaction waves propagate, pores partially or fully close; hence, the density of fringes changes, which leads to a gray-level change in the images. While this change is clearly evidenced behind the compaction front, it is barely detectable across the elastic precursor. To improve this detection, the first (static) radiograph was subtracted to the four next. Thus, for each shot, the top sequence provides raw radiographs showing the propagation of the compaction wave (red arrow), while in the bottom sequence, the first image was subtracted to the others, in order to visualize

TABLE III. Experimental and calculated data for eSRF shots. p_{cal} is the maximum ablation pressure calculated using the analytical model [Eq. (1)] with $\alpha = 0.2$ for water confinement and $\alpha = 0.15$ for glass confinement. c_{exp} and $U_{S,exp}$ are the mean celerities of elastic and compaction waves inferred from *in situ* radiography, and $U_{S,cal}$ is a model prediction.

Shot	Intensity I_0 (GW/cm^2)	Pressure P_{cal} (GPa)	Elastic wave celerity	Compaction wave celerity	
			C_{exp} (m/s)	Experimental $U_{S,exp}$ (m/s)	Calculated $U_{S,cal}$ (m/s)
#1	4.95 ± 0.18	1.37 ± 0.02	…	…	…
#2	5.38 ± 0.19	1.43 ± 0.03	1272 ± 150	551 ± 30	517
#3	5.38 ± 0.19	1.43 ± 0.03	…	…	…
#4	2.69 ± 0.10	1.01 ± 0.02	…	…	…
#6	8.06 ± 0.52	1.75 ± 0.06	986 ± 130	395 ± 25	559
#7	8.59 ± 0.55	1.74 ± 0.06	1070 ± 140	329 ± 20	545
#9	5.67 ± 0.31	1.41 ± 0.04	1243 ± 150	404 ± 25	475
#10	1.32 ± 0.07	0.68 ± 0.02	…	…	…

the elastic wave front (black arrow). For all shots, the resolution is not high enough to quantify wave fronts thicknesses.

The positions of the wave fronts inferred from the successive radiographs are plotted in Fig. 9. Error bars were evaluated by accounting for uncertainties on the front positions and imperfect planarity of the fronts, likely to be due to (i) non-uniform pressure load, (ii) material inhomogeneous mesostructure, and (iii) edge effects, i.e., lateral release waves coming from the periphery of the loaded spot where laser energy and subsequent ablation pressure decrease gradually with the radial distance. Thus, the uncertainty on the location of the shock front can be several pixels and, thus, several tens of μm. Within these error bars, the elastic wave velocity is found to be basically constant over the duration of observation (Fig. 9). On the other hand, the compaction wave velocity decreases slightly with propagation distance, which is consistent with the expected decay of a compressive pulse traveling in a porous medium. Mean velocities are listed in Table III. Whereas the elastic wave velocity is roughly identical for all shots, within experimental uncertainties mentioned above, the celerity of the compaction wave depends on the level of pressure reached into the foam.

These observations are qualitatively similar to those obtained in previous dynamic experiments performed on other polymeric foams. Ravindran *et al.*,[30] for example, performed gas gun experiments on a low density polymeric foam (154 kg/m^3), coupled with ultra-fast imaging and digital image correlation. They showed that an elastic precursor propagated first at a velocity of 740 m/s, followed by a compaction wave at a relatively low velocity of around 139 m/s. Song *et al.*[31] also demonstrated the propagation of two waves, the first elastic one propagating at 348 m/s and the second plastic one at 37 m/s, in an epoxy foam (120 kg/m^3) subjected to SHPB tests. The main difficulty in SHPB tests is due to the very low impedance of foams, resulting in a late state of stress equilibrium. This limits the sample thickness and impact velocity that can be used.[30,32]

One would expect an increase of the compaction wave velocity with the pressure applied, which is not the case. This discrepancy can have two explanations. The first one is the laser breakdown in the confining layer, which, as explained in the Sec. IV A, induces a saturation of the ablation pressure and a shortening of the pulse so that the pressure loads in shots #6 and #7, where laser intensity exceeds 8 GW/cm^2, might be overestimated. The second explanation is that if the laser spot diameter is small compared to propagation distances (as in shots #6 and #7), lateral release waves quickly catch up with the shock wave. Thereafter, conditions of uniaxial strain are no longer valid so that the measured velocity is not that of a planar compaction wave. This will be confirmed in Sec. V B.

For thin samples, it is possible to measure the mean velocity of the rear free surface upon the breakout of the elastic wave, and deduce the Hugoniot Elastic Limit (HEL) of the foam (i.e., the amplitude of the elastic wave or so-called dynamic yield strength), given by the following formula:

$$\mathrm{HEL} = \frac{1}{2}\rho_0 C V_{FS}, \tag{3}$$

where ρ_0 is the initial density of the foam, C is the celerity of the elastic wave, and V_{FS} is the velocity of the free surface. As illustrated in Fig. 10, the displacement of the bottom surface of the foam sample [Fig. 10(a)] for shot #9 can be plotted as a function of time [Fig. 10(b)]. This gives a roughly constant free surface velocity V_{FS} of 128 ± 20 m/s, leading to a HEL stress of 25 ± 9 MPa, which is in agreement with the one evaluated by Mane *et al.*[4] in a polyurethane foam of density 288 kg/m^3, tested on a drop weight tower (HEL ~24 MPa). It is also consistent with our own previous work.[16–18] In shot #6, because the rear surface was maintained with a tape for recovery and for post-shot analyzes, the above formula does not apply.

After the propagation of the compaction wave, radiographs suggest a partial reversion of the deformation. The structure of the foam seems to have been preserved (no or little damage). However, radiographs alone cannot confirm this hypothesis. Indeed, the image captured by the CCD camera integrates images of undeformed material and deformed material since lateral dimensions of the samples are greater than the laser spot [see Fig. 4(b)].

C. Post-shot tomography

Recovered foam samples were observed using scanning electron microscopy (SEM) and X-ray tomography, to analyze damage mechanisms involved during and after shock and release waves

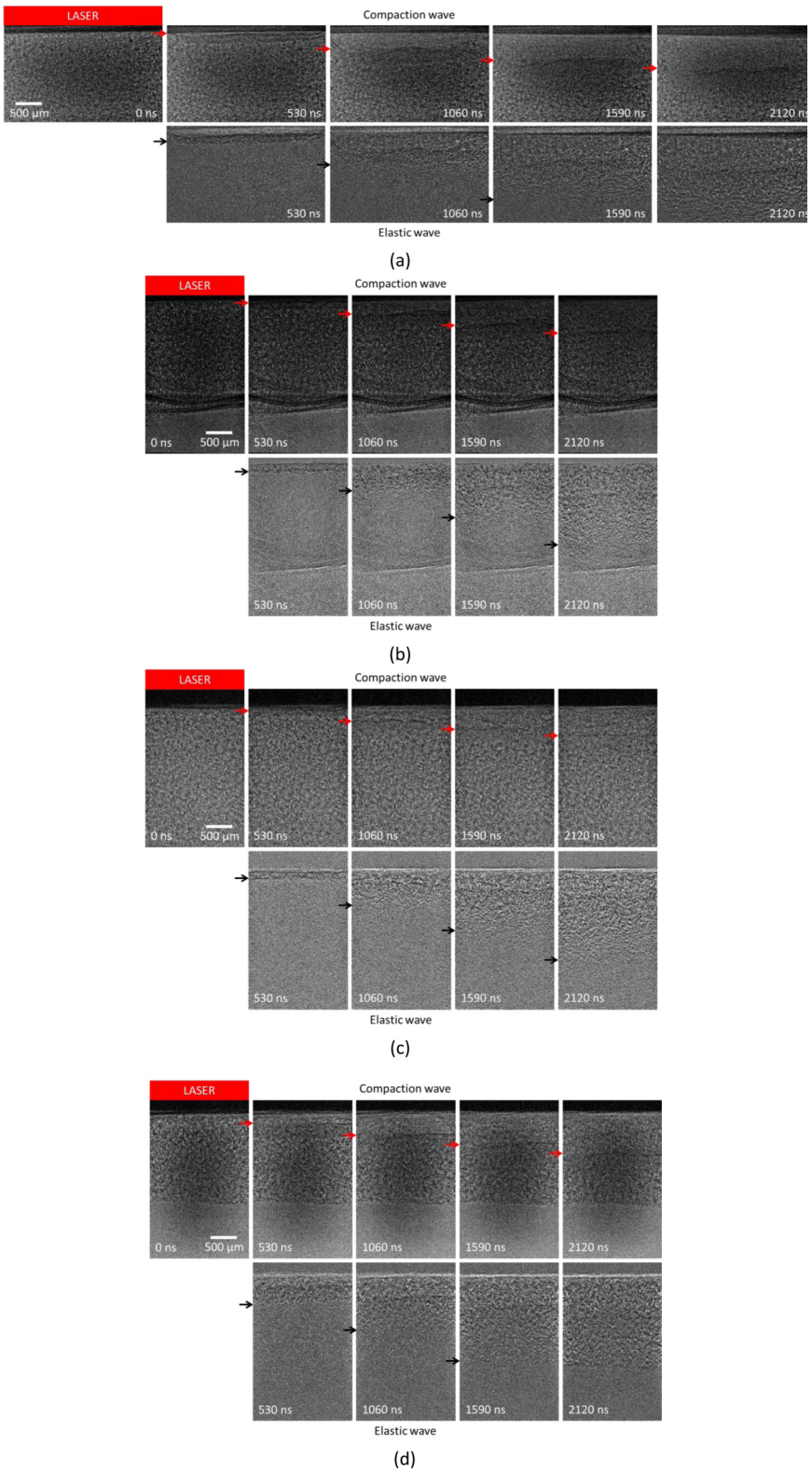

FIG. 8. Time sequences of x-ray radiographs of foam samples subjected to laser shock loading on their top surface, for shots #2 (a), #6 (b), #7 (c), and #9 (d). The top row shows raw radiographs, with the position of the compaction front (red arrows), while in the bottom row, the first (static) image was subtracted from the four next to help visualize the elastic wave front (black arrows).

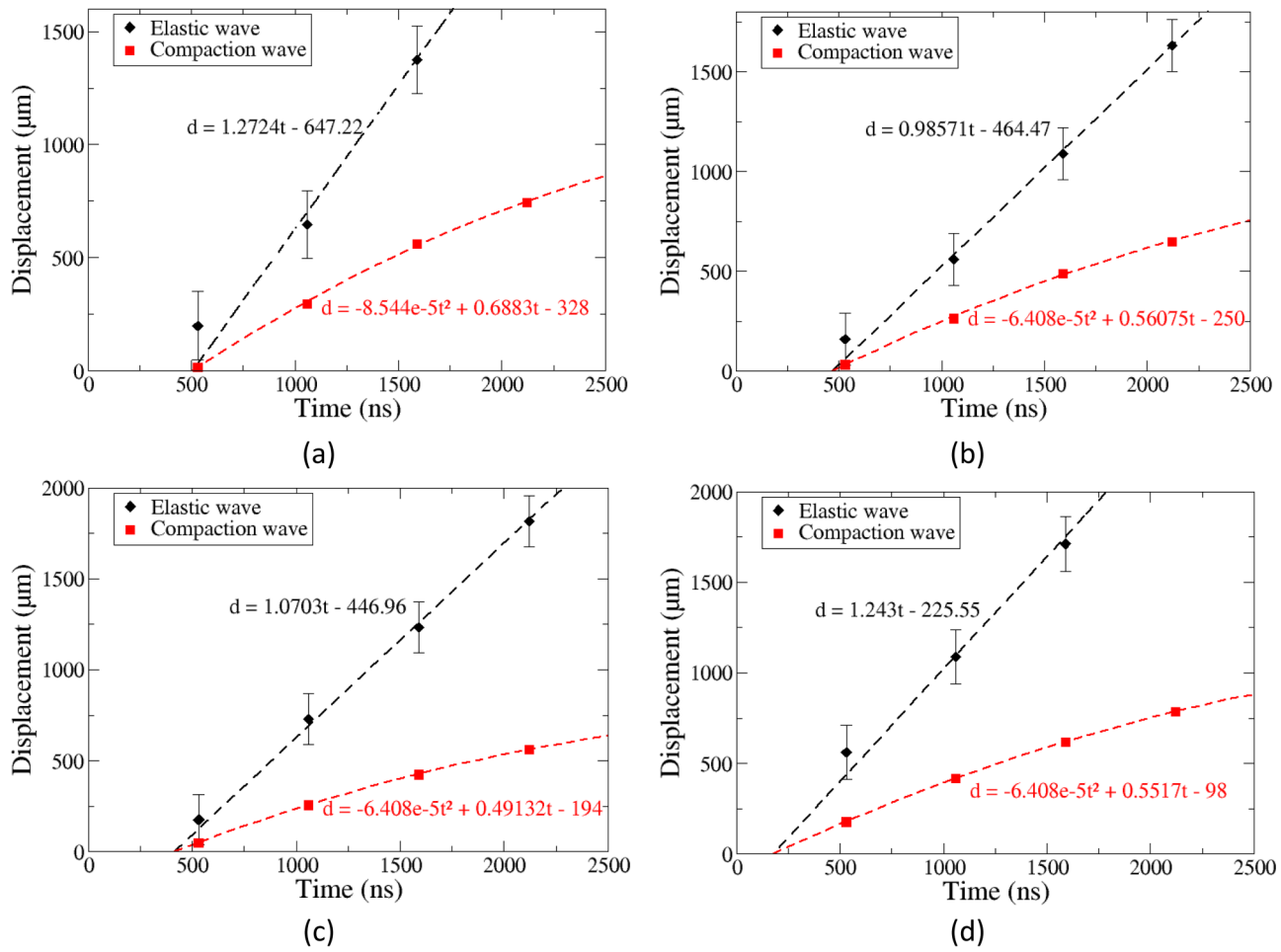

FIG. 9. Evolution of the displacement of elastic and compaction waves as a function of time for shots 2 (a), 6 (b), 7 (c), and 9 (d).

propagation. Tomographs of the sample from shot #3 suggest brittle failure of the cell walls, so that the foam is actually partially compacted below the loaded surface (Fig. 11). The width of the damaged area matches the diameter of the loaded area. Considering the foam mesostructure (large pores) and the large propagation distances, it is clear that the assumption of a propagation of planar wave fronts is a rough, highly idealized picture. For instance, Koohbor *et al.*[33] studied differences in the local and global strain response at failure in a rigid closed-cell polyurethane foam. They found that depending on the strain rate applied locally on the foam, and cell walls thicknesses, failure modes changed from elastic buckling to brittle failure. They showed that local strain rates were one order of magnitude higher than global ones. These higher local strain rates result in the hardening of the polymeric matrix, modifying the small-scale failure mode. In our study, the pressure reached in the foam and the strain rate (about 10^6 s^{-1}) are so high that the main failure mechanism is brittle failure.

Figure 12 shows a SEM view of a foam sample recovered after a high pressure laser shot performed at the Institut Pprime, for an energy of 7.5 J, 5 mm diameter spot, with water confinement. The sample was perforated, leaving a central hole of similar diameter as that the loaded spot. The micrograph shows the edge of this large hole, and confirms the brittle behavior of the polymer, with cell edges breaking "like eggshells."

This high-velocity behavior contrasts with the low strain-rate response. Figure 13 shows an *in situ* tomograph of a foam sample subjected to a quasi-static compression performed up to 12.5 MPa at the Institut Pprime. At these strain rates, pores can partially close with high deformation of cell edges, buckling without failure. In that case, partial volume recovery was observed after unloading to ambient pressure. This clearly shows the strain-rate dependence of damage mechanisms involved in the foam. These results are in good agreement with the observations of Koohbor *et al.*,[33] who showed that for thinner cell walls, which is the case in the studied

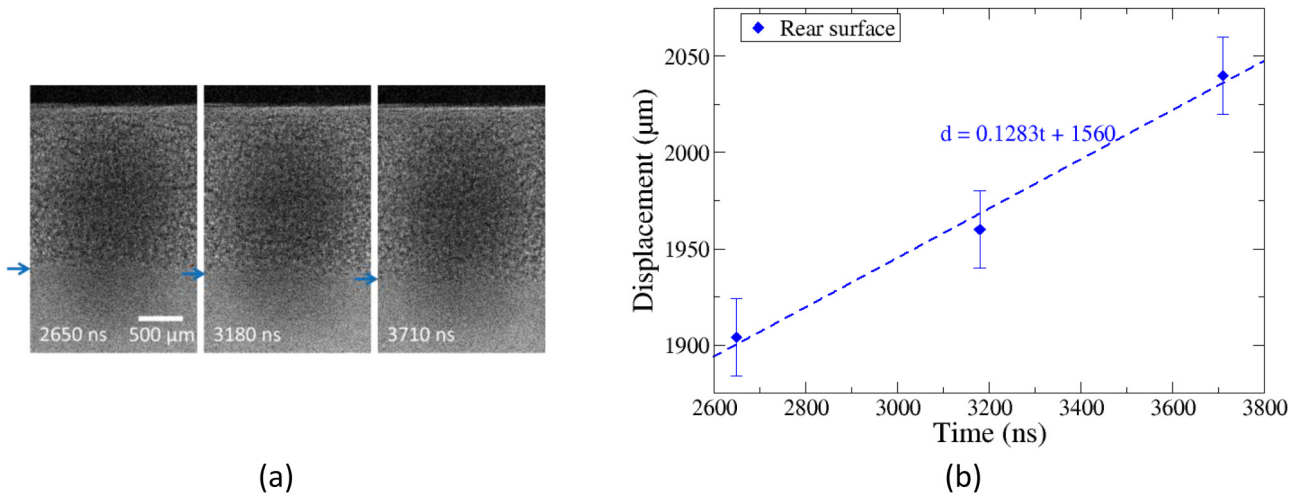

FIG. 10. Radiographs showing the displacement of the rear surface of the foam sample for the shot #9 (a) and evolution of this displacement as a function of time (b).

foam with an approximate cell wall size of 30 μm, the main failure mode under quasi-static loading is due to elastic buckling.

V. MODELING

A. Constitutive model

To model the macroscopic dynamic behavior of the foam, the POREQST compaction model, developed by Seaman *et al.*,[34] was implemented into a CEA-homemade explicit 1D Lagrangian hydrocode. The model is defined by an equation of state (EOS) for the dense material (i.e., constituting the foam matrix), a compaction curve, a fracture curve, and a constitutive law for the partially compacted material (Fig. 14). The initial elastic curve (1) is described by Hooke's relations using the initial bulk modulus K_0 and the initial density ρ_0 of the foam. The equilibrium compaction curve (2) is defined by a piecewise-polynomial function. The equilibrium compaction curve and the initial elastic curve intersect at the HEL. Below the HEL, the main deformation mechanism is the

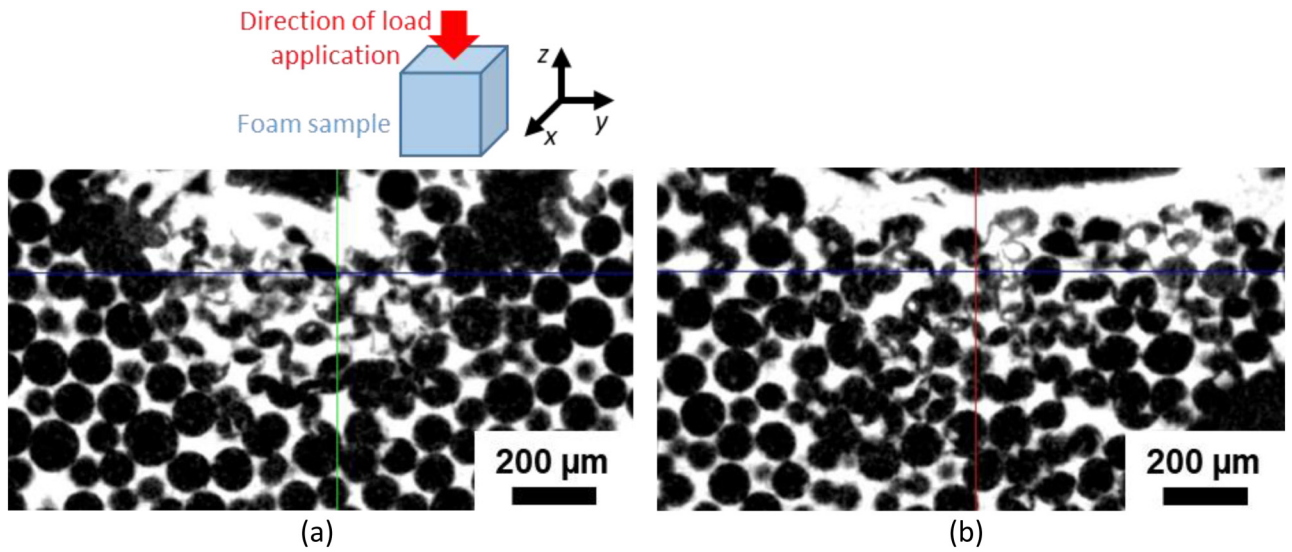

FIG. 11. Two sections in *yz* (a) and *xz* (b) orthogonal planes extracted from post-shock x-ray tomography of the foam sample recovered after the laser shot #3 at the ESRF, in water-confined geometry (E = 3.8 J, D = 3 mm).

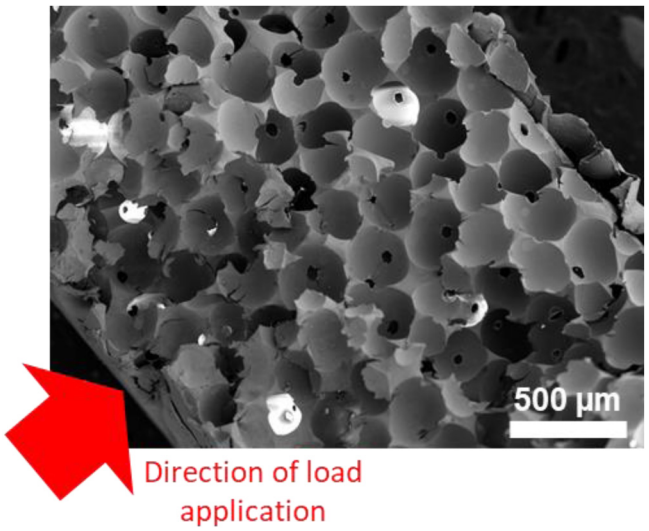

FIG. 12. SEM observation of a foam sample, recovered after a high pressure laser shot performed at the Institut Pprime ($E = 7.5$ J, $\Phi = 5$ mm).

elastic bending of cell edges. Above the HEL, compaction is due to foam matrix buckling and then cells crushing. Due to viscoplastic effects, shock-compressed states actually lie on a dynamic compaction curve (3). The pressure-density law of the dense material (4) is described by a Mie–Grüneisen EOS. Unloading from partially densified states occurs along elastic release paths (5). Further

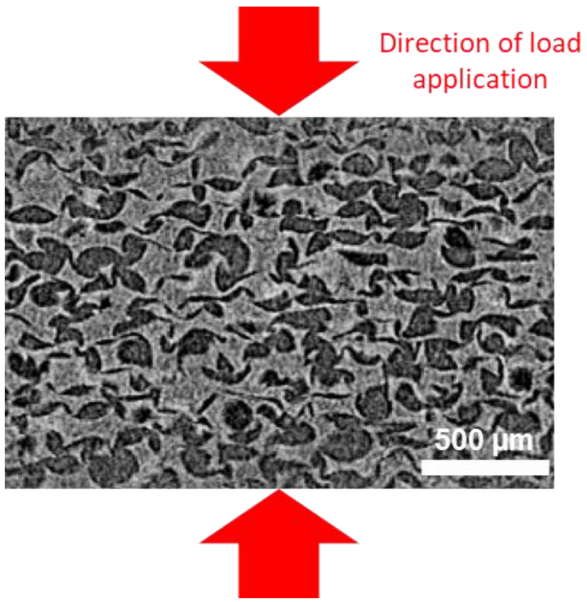

FIG. 13. *In situ* tomograph of a foam sample subjected to a quasi-static compression.

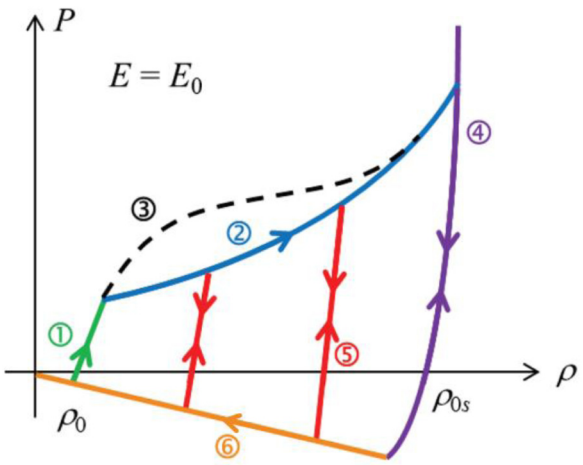

FIG. 14. Schematic of the POREQST compaction model. It describes the initial elastic behavior of the porous material (1), the compaction via an equilibrium compaction curve (2), and the densification using a Mie–Grüneisen EOS (4). After release on intermediate state curve (5), tensile stresses could be applied to the foam. If the release is sufficient, damage can occur and the re-opening of cells is driven by the damage curve (6). In order to take into account viscoplasticity, a dynamic compaction curve is also implemented (3).

rarefaction can take the foam into tension, which can produce cell re-opening driven along a damage curve (6).

For the polyurethane foam, model parameters were calibrated using magnetic pressure tests, and plate impact experiments.[16] The model was also validated to some extent by performing electron beam tests and laser-driven shock experiments.[17,18] The elastic wave celerity depends on the initial foam density ρ_0 and the bulk modulus K_0. The calibration of model parameters gives $K_0 = 500$ MPa; thus, the elastic wave celerity is $C_0 = \sqrt{K_0/\rho_0} = 1250$ m/s. The compaction wave celerity depends on the compaction curve shape. In this model, the HEL is about 21 MPa.

B. Numerical results

The above model was used to simulate the macroscopic response of the foam to laser-driven shock compression, using the pressure history in the aluminum plasma as input boundary condition applied onto the sample surface. Peak loading pressures were inferred from Eq. (1) (see Table III) and temporal shapes of the pressure pulses were estimated from the calibration tests [e.g., Fig. 6(a)]. However, because the laser pulse duration in these tests was about 25–30 ns FWHM against 10–12 ns in the ESRF experiments, the pressure pulse duration was shortened accordingly from 50 ns FWHM [Fig. 6(a)] to 20 ns.

Figure 15(a) is a typical time–distance plot from the simulation of shot #2. It shows the propagation from the loaded surface at time 0 of an elastic wave of constant velocity, compressing the foam to the HEL pressure of 21 MPa (green), followed by a slower compaction wave of decreasing velocity inducing further compression to about 1 GPa (blue), before gradual unloading to ambient pressure (red). As stated earlier, the elastic wave propagates at

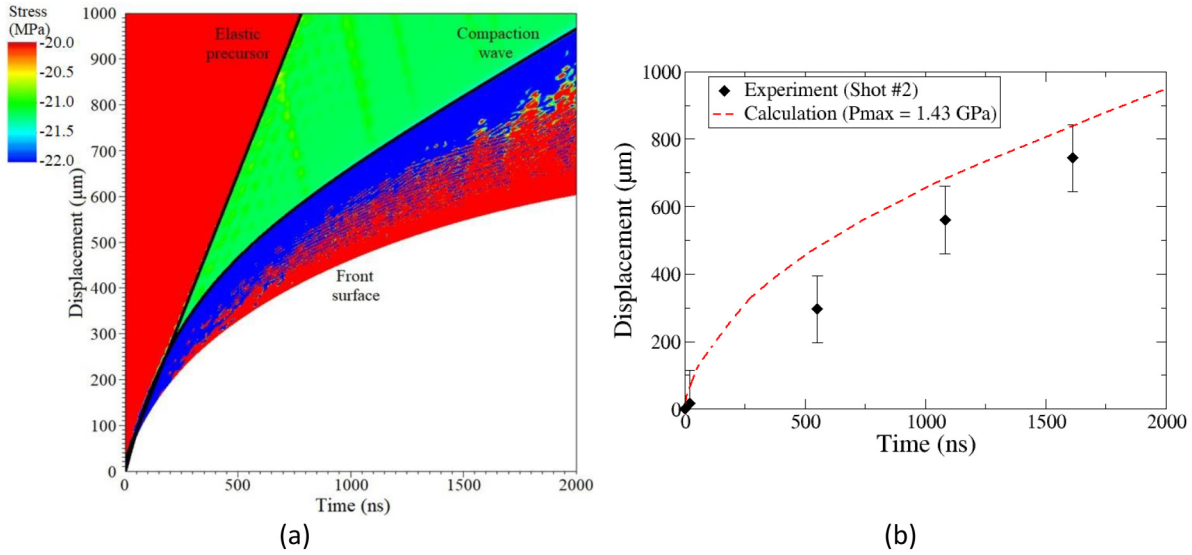

FIG. 15. Simulation of the ESRF experiment #2. (a) Distance–time diagram showing wave propagation, with pressure contours bounded between 20 MPa (red) and 22 MPa (blue), and (b) computed trajectory of the compaction wave (red) compared with that inferred from the corresponding radiographs (black).

1250 m/s, which is in good agreement with the radiographs (Table III). In Fig. 15(b), the trajectory of the compaction wave in the simulation is compared with that inferred from the corresponding radiographs [Fig. 8(a) and Fig. 9(a), shifted so that displacement starts at time 0]. Both curves are fairly parallel at late times (i.e., wave velocities are similar) but the first acceleration is much steeper in the simulation. This is probably because considering the foam as a continuous, homogeneous medium is a very rough way to capture its early response to the very sharp compressive pulse just beneath the loaded surface. Similar trends are found for all shots, although the discrepancy between computed and measured trajectories is stronger for shots #6 and #7. The comparison between measured and calculated mean celerities of the compaction wave is shown in Table III. For shots #2 and #9, calculated velocities are fairly consistent with those determined experimentally. On the other hand, for shots #6 and #7, calculated velocities are about 50% higher than in the experiments. The first and the most probable reason explaining this overestimation is laser breakdown for these high intensity shots. As specified in Sec. IV A, this phenomenon has the consequence to saturate the peak pressure and reduce the pulse duration. Thus, loading pressures in Table III are most likely overestimated for these two shots. Another reason can be edge effects, which are not taken into account in our simulations. They consist in lateral release waves, which interact with the compaction wave, so the velocity measured over long propagation distances is no longer that of a planar wave.

VI. CONCLUSIONS

Laser-driven shock experiments, coupled with original *in situ* x-ray imaging were conducted in a synchrotron facility to investigate the dynamic response of polyurethane foam. They allowed the time-resolved observation of both elastic wave and slower compaction wave propagating from the loaded surface. In addition, post-shock x-ray tomography of the recovered samples, complemented with observations under quasi-static compression, provided an insight into the rate-dependent mechanisms governing pore collapse. The ablation pressure on the front surface of the foam samples was estimated from an analytical model of laser–matter interaction, comforted by calibration shots performed under analogous irradiation conditions. The resulting pressure loads were used as input data for 1D hydrodynamic simulations where the foam was modeled with a macroscopic constitutive law accounting for dynamic compaction. Differences between calculated and measured wave velocities can be explained by (i) the limitations of this macroscopic approach, (ii) edge effects in the cases of small loaded surfaces, and (iii) laser breakdown likely to have occurred in some high intensity shots.

ACKNOWLEDGMENTS

We thank Yann Rouchausse (PIMM) for technical support during the preparation of the experiment, and Marc Castaing and Thales LAS for allowing us to use their laser. This work was partially funded by the French Government program "Investissements d'Avenir" (EQUIPEX GAP, Reference No. ANR-11-EQPX-0018).

AUTHOR DECLARATIONS

Conflict of Interest

The authors have no conflicts to disclose.

DATA AVAILABILITY

The data that support the findings of this study are available from the corresponding author upon reasonable request.

REFERENCES

[1]L. J. Gibson and M. F. Ashby, *Cellular Solids Structure and Properties, Cambridge Solid State Science Series*, 2nd ed. (Cambridge University Press, 1997).
[2]V. P. W. Shim and K. Y. Yap, "Modelling impact deformation of foam-plate sandwich systems," Int. J. Impact Eng. **19**, 615–636 (1997).
[3]V. P. W. Shim, Z. H. Tu, and C. T. Lim, "Two-dimensional response of crushable polyurethane foam to low velocity impact," Int. J. Impact Eng. **24**, 703–731 (2000).
[4]J. V. Mane, S. Chandra, S. Sharma, H. Ali, V. M. Chavan, B. S. Manjunath, and R. J. Patel, "Mechanical property evaluation of polyurethane foam under quasi-static and dynamic strain rates- an experimental study," Procedia Eng. **173**, 726–731 (2017).
[5]E. Linul, D. A. Şerban, L. Marsavina, and T. Sadowski, "Assessment of collapse diagrams of rigid polyurethane foams under dynamic loading conditions," Arch. Civil Mech. Eng. **17**, 457–466 (2017).
[6]W. Chen, F. Lu, and N. Winfree, "High-strain-rate compressive behavior of a rigid polyurethane foam with various densities," Exp. Mech. **42**, 65–73 (2002).
[7]L. M. Yang and V. P. W. Shim, "A visco-hyperelastic constitutive description of elastomeric foam," Int. J. Impact Eng. **30**, 1099–1110 (2004).
[8]A. Pellegrino, V. L. Tagarielli, R. Gerlach, and N. Petrinic, "The mechanical response of a syntactic polyurethane foam at low and high rates of strain," Int. J. Impact Eng. **75**, 214–221 (2015).
[9]D. Whisler and H. Kim, "Experimental and simulated high strain dynamic loading of polyurethane foam," Polym. Test. **41**, 219–230 (2015).
[10]P. Li, Y. B. Guo, M. W. Zhou, and V. P. W. Shim, "Response of anisotropic polyurethane foam to compression at different loading angles and strain rates," Int. J. Impact Eng. **127**, 154–168 (2019).
[11]N. Lelong and D. Rochais, "Influence of microstructure on the dynamic behavior of a polyurethane foam with the material point method," Materialia **5**, 100199 (2019).
[12]E. Zaretsky, Z. Asaf, E. Ran, and F. Aizik, "Impact response of high density flexible polyurethane foam," Int. J. Impact Eng. **39**, 1–7 (2012).
[13]R. Nasirzadeh and A. R. Sabet, "Study of foam density variations in composite sandwich panels under high velocity impact loading," Int. J. Impact Eng. **63**, 129–139 (2014).
[14]B. Koohbor, A. Kidane, W.-Y. Lu, and M. A. Sutton, "Investigation of the dynamic stress–strain response of compressible polymeric foam using a non-parametric analysis," Int. J. Impact Engineering **91**, 170–182 (2016).
[15]A. Taherkhani, M. Sadighi, A. S. Vanini, and M. Z. Mahmoudabadi, "An experimental study of high-velocity impact on elastic–plastic crushable polyurethane foams," Aerosp. Sci. Technol. **50**, 245–255 (2016).
[16]P. Pradel, F. Malaise, T. de Rességuier, C. Delhomme, G. Le Blanc, and J. H. Quessada, "Dynamic compaction of polyurethane foam: Experiments and modelling," Eur. Phys. J.: Spec. Top. **227**, 3–16 (2018).
[17]P. Pradel, F. Malaise, T. de Rességuier, C. Delhomme, B. Cadilhon, J.-H. Quessada, and G. Le Blanc, "Stress wave propagation and mitigation in two polymeric foams," AIP Conf. Proc. **1979,** 110015 (2018).
[18]P. Pradel, F. Malaise, and T. de Rességuier, "Laser-driven shock experiments to investigate mitigation ability of polymeric foams," EPJ Web Conf. **183**, 01045 (2018).
[19]S. P. Marsh, in *LASL Shock Hugoniot Data*, edited by S. P. Marsh (University of California Press, Berkeley, 1980).
[20]M. P. Olbinado, V. Cantelli, O. Mathon, S. Pascarelli, J. Grenzer, A. Pelka, M. Roedel, I. Prencipe, A. L. Garcia, U. Helbig, D. Kraus, U. Schramm, T. Cowan, M. Scheel, P. Pradel, T. de Rességuier, and A. Rack, "Ultra high-speed x-ray imaging of laser-driven shock compression using synchrotron light," J. Phys. D: Appl. Phys. **51**, 055601 (2018).
[21]M. P. Olbinado, X. Just, J.-L. Gelet, P. Lhuissier, M. Scheel, P. Vagovic, T. Sato, R. Graceffa, J. Schulz, A. Manusco, J. Morse, and A. Rack, "MHz frame rate hard X-ray phase-contrast imaging using synchrotron radiation," Opt. Express **25**, 13857–13871 (2017).
[22]P. Cloetens, R. Barrett, J. Baruchel, J.-P. Guigay, and M. Schlenker, "Phase objects in synchrotron radiation hard x-ray imaging," J. Phys. D: Appl. Phys. **29**, 133–146 (1996).
[23]L. Berthe, R. Fabbro, P. Peyre, L. Tollier, and E. Bartnicki, "Shock waves from a water-confined laser-generated plasma," J. Appl. Phys. **82**, 2826–2832 (1997).
[24]R. Fabbro, J. Fournier, P. Ballard, D. Devaux, and J. Virmont, "Physical study of laser-produced plasma in confined geometry," J. Appl. Phys. **68**, 775–784 (1990).
[25]D. Devaux, R. Fabbro, L. Tollier, and E. Bartnicki, "Generation of shock waves by laser-induced plasma in confined geometry," J. Appl. Phys. **74**, 2268–2273 (1993).
[26]A. Sollier, Ph.D. thesis, Versailles St-Quentin University, 2002.
[27]L. Berthe, R. Fabbro, P. Peyre, and E. Bartnicki, "Wavelength dependent of laser shock-wave generation in the water-confinement regime," J. Appl. Phys. **85**, 7552–7555 (1999).
[28]W. L. Smith, J. H. Bechtel, and N. Bloembergen, "Picosecond laser-induced breakdown at 5321 and 3547 Å: Observation of frequency-dependent behavior," Phys. Rev. B **15**, 4039–4055 (1977).
[29]M. A. Meyers, *Dynamic Behavior of Materials* (John Wiley & Sons, Ltd, 1994).
[30]S. Ravindran, B. Koohbor, P. Malchow, and A. Kidane, "Experimental characterization of compaction wave propagation in cellular polymers," Int. J. Solids Struct. **139–140**, 270–282 (2018).
[31]B. Song, M. J. Forrestal, and W. Chen, "Dynamic and quasi-static propagation of compaction waves in a low-density epoxy foam," Exp. Mech. **46**, 127–136 (2006).
[32]V. S. Deshpande and N. A. Fleck, "High strain rate compressive behaviour of aluminium alloy foams," Int. J. Impact Eng. **24**, 277–298 (2000).
[33]B. Koohbor, S. Ravindran, and A. Kidane, "Effects of cell-wall instability and local failure on the response of closed-cell polymeric foams subjected to dynamic loading," Mech. Mater. **116**, 67–76 (2018).
[34]L. Seaman, R. E. Tokheim, D. R. Curran, "Computational representation of constitutive relations for porous materials," Technical Report, Stanford Research Institute, 1974.